energies

MDPI

Article

Numerical Modeling of Bifacial PV String Performance: Perimeter Effect and Influence of Uniaxial Solar Trackers

Fabio Ricco Galluzzo [1,2,*]**, Pier Enrico Zani** [3]**, Marina Foti** [3]**, Andrea Canino** [3]**, Cosimo Gerardi** [3] **and Salvatore Lombardo** [1,*]

[1] Istituto per la Microelettronica e Microsistemi—Consiglio Nazionale delle Ricerche, Zona Industriale, Ottava Strada n. 5, 95121 Catania, Italy

[2] Dipartimento di Fisica e Astronomia, Università di Catania, Via S. Sofia, 64, 95123 Catania, Italy

[3] ENEL Green Power, Contrada Blocco Torrazze—Z.I., 95121 Catania, Italy; zanipierenrico@gmail.com (P.E.Z.); marina.foti@enel.com (M.F.); andrea.canino@enel.com (A.C.); cosimo.gerardi@enel.com (C.G.)

[*] Correspondence: Fabioricco.Galluzzo@imm.cnr.it (F.R.G.); salvatore.lombardo@imm.cnr.it (S.L.)

check for updates

Abstract: The bifacial photovoltaic (PV) systems have recently met large interest. The performance of such systems heavily depends on the installation conditions and, in particular, on the albedo radiation collected by the module rear side. Therefore, it is of crucial importance to have an accurate performance model. To date, in the scientific literature, numerous models have been proposed and experimental data collected to study and optimize bifacial PV system performance. Currently, 3D and 2D models of bifacial PV devices exist. Though the former are more mathematically complex, they can lead to more accurate results, since they generally allow to fully consider the main aspects influencing a bifacial PV system performance. Recently, we have proposed and validated through experimental data a 3D model tested as a function of module height, tilt angle, and ground albedo. In this work, through such a model, we studied the role played by the perimeter zones surrounding the PV string, by considering PV strings of 30 or 60 modules. We considered the cases of fixed installation with optimal PV module tilt and of installation with uniaxial horizontal solar tracker. We evaluated the PV energy yield as a function of the size of the perimeter zones for the two cases, i.e., both with and without the solar tracker. In optimal perimeter conditions, we then studied the behavior of bifacial and mono-facial PV strings by varying the geographical location in a large latitude range.

Keywords: bifacial PV modeling; perimeter effect; solar tracker influence

1. Introduction

Bifacial photovoltaic (PV) systems are now becoming of large interest because of their high potential of PV energy yield. In fact, a considerable and rapid development with a remarkable market share growth (up to over 35% in 2028) is foreseen for bifacial PV modules [1].

The bifacial PV module performance heavily depends on the installation conditions and on the albedo radiation which the module rear side can collect. Therefore, it is of crucial importance to model the performance of such devices as accurately as possible, by considering the different variables influencing it.

To date, numerous models have been proposed and experimental data collected to study and optimize the performance of bifacial PV systems. Both three-dimensional (3D, see Reference [2–10]) and two-dimensional (2D, see, for instance, Reference [11–13]) models of bifacial PV devices have been proposed. Though the former are more mathematically complex, they can, in principle, lead to more accurate results taking into account more closely the PV system geometry. Recently, we proposed a

3D model [10], and we compared its results with experimental data. Such data were taken in Catania (37°26′32″ N, 15°3′47″ E), by using a mini-module of 4 series-connected bifacial PV cells realized in a n-type passivated emitter rear totally diffused (nPERT) technology [14], with an asphalt ground and in clear sky conditions. To evaluate different albedo conditions, we also mounted the PV mini-module above a white plastic sheet, and we varied the position of the white sheet with respect to the module. We, therefore, studied the behavior of the bifacial PV module as a function of tilt angle, ground albedo, and module elevation from the ground. We observed that, to achieve good agreement between model and data, it is important to consider the incidence angle of the light on the module surface. In fact, the module glass reflectivity R tends to 100% for grazing light incidence, as the incidence angle θ tends to 90°, as well known from the Fresnel reflectivity equations. As a simplifying hypothesis, rather than using the reflectivity as calculated from the Fresnel equations, we assumed that, for θ ≥ 80°, R is 100%, i.e., no light enters into the PV module. We, therefore, took into account that the diffused light coming from ground zones far from the module is not collected by the PV module being reflected. Through such modeling, we achieved an accurate description of the module performance as a function of the module elevation from the ground, of the tilt angle, and of the ground albedo, consistent with the experimental data [10].

In this work, we started from the aforementioned model, tuned to experimental data, and, through this, we studied the role played by perimeter zones, by considering photovoltaic strings of 30 or 60 modules for both the cases of fixed installation (with PV modules optimally tilted) and of PV string equipped with uniaxial horizontal solar tracker. In fact, the PV modules in the central part of the string are expected to have a very different behavior compared to the edge modules since their backside illumination will be different. The other investigated aspect is the impact of the use of horizontal solar trackers, an issue not yet well studied in the case of bifacial PV modules. Indeed, although several studies in the literature analyzed the effect due to solar trackers on a traditional mono-facial PV system and solar collector performance (for instance, see Reference [15–28]), currently few studies exist (see Reference [29–31]) for bifacial PV systems, and further studies are required. Such a need arises because, for a bifacial system, the benefit on the performance determined by the use of solar trackers could be sensibly different from that observed on traditional mono-facial PV systems. In fact, the performance of a bifacial PV system is determined also by its rear side performance, and the solar radiation optimization on its front side through a traditional type of solar tracker could not ensure an overall optimization of the system performance. For both cases (with and without tracker), we demonstrate in the following that the perimeter zones of the ground have a relevant effect on the performance of the bifacial PV string.

In the final part of the paper, the performance of bifacial PV strings by varying the geographical location is also studied, by considering both the cases of fixed string (with module tilt angle equal to the latitude of each considered location) and of string with uniaxial solar tracker, in a large range of latitudes. We show that the PV energy yield gain due to the adoption of the horizontal solar tracker compared to the one of a fixed string decreases by increasing the latitude of the installation site, both for a bifacial PV string and for a mono-facial one. Furthermore, our results show that the PV energy yield with the tracker is higher for the mono-facial PV strings compared to the bifacial PV string (as consistent with the results in Reference [29]). The results of our work contribute to quantify the advantage in terms of energy generated by a bifacial PV string, achievable through the mentioned type of solar tracker at different geographical locations.

The structure of this work consists of the first part (Section 2), where the applied methods and the proposed model are described in detail; and the second part (Section 3), where the main simulation results are illustrated and discussed. Finally, the main conclusions are highlighted in Section 4.

2. Methods and Model Description

Figure 1 shows schematics of the PV module placement geometry, for both the cases considered in the present study, of fixed PV string (Figure 1a) and of PV string with uniaxial horizontal solar tracker

(Figure 1b). In both cases, two module rows are considered. For the fixed PV string, the rows are along the direction east–west and the modules are oriented towards the south, since only geographical locations of the northern terrestrial hemisphere are considered in this study. Moreover, the PV modules of the fixed string have a tilt angle equal to the latitude of the geographical location considered, since this is known to be the optimal tilt angle in the case of mono-facial and bifacial PV modules ([8,32]). For the string with horizontal tracker, the two rows are along the tracker rotation axis, oriented along the north–south direction. The considered PV strings consist of 30 or 60 modules; hence, each row can contain 15 or 30 modules.

(**a**) (**b**)
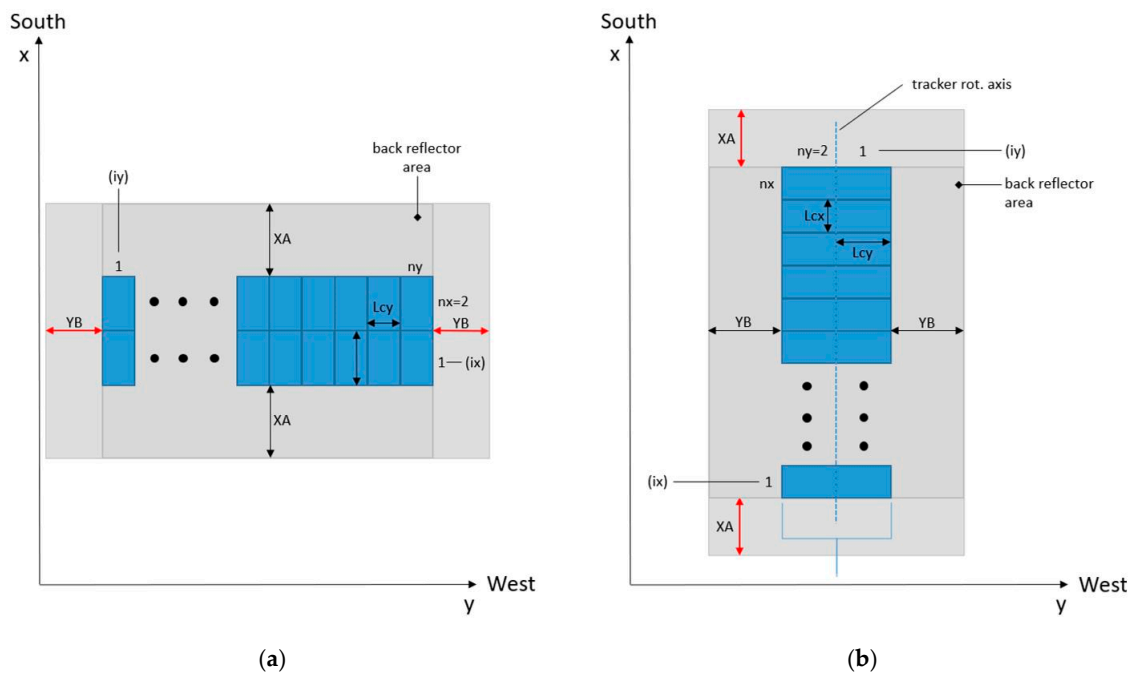
Figure 1. Module placement geometry for the two cases considered in this study: (**a**) fixed photovoltaic (PV) string, with modules oriented towards south and tilted of an angle equal to the latitude of the considered location of the northern terrestrial hemisphere; (**b**) PV string with uniaxial horizontal solar tracker. XA and YB are the parameters identifying the dimensions of the ground zone (acting as back reflector for the bifacial PV devices) considered for the calculations. nx represents the total number of PV modules along the x direction, i.e., the north–south direction (equal to 2 for the fixed string, 15 or 30 for the string with tracker), while ny indicates the total number of PV modules along the y direction, i.e., the east–west direction (equal to 15 or 30 for the fixed string, 2 for the string with tracker). For the main purpose of studying the perimeter effects, in this work, YB was varied (by assuming for it the values 0, 5, 10, or 20 m, alternately) with XA constant (equal to 5 m) for the fixed string; instead, for the PV string with tracker, XA was varied (by assuming for it the values 0, 5, 10, or 20 m, alternately) with YB constant (equal to 5 m).

To individuate the PV modules within the string, we use the following notation: x and y indicate the directions along the meridian and the parallel passing through the geographical location considered, respectively; the corresponding module indices are named ix and iy, respectively. Therefore, for the case of fixed string, ix varies between 1 and 2, and iy varies between 1 and 15 (or 30). For the string with tracker, ix varies between 1 and 15 (or 30), and iy varies between 1 and 2.

Regarding the 3D model used in the present study, in order to estimate the incident radiation on the PV module surfaces, we firstly calculate the azimuth and zenith angles of the sun as a function of time, as described in detail in Reference [33]. Days are numbered from 1 to 365, corresponding to January 1st and December 31st, respectively. The global solar radiation is divided into the direct (beam), diffuse, and reflected components. Such components are modeled by using the ASHRAE

model [34], corrected by the more recent Global Solar Atlas database [35], and the isotropic Liu and Jordan's model [36].

Therefore, the global irradiance (I_{front}) on a PV module front surface inclined of a tilt angle equal to $β$, is evaluated according to the equation below [37]:

$$I_{front} \; = \; I_{b,β} + I_{d,β} + I_{r,β} \tag{1}$$

being $I_{b,β}$, $I_{d,β}$, and $I_{r,β}$, the beam, diffuse, and reflected components of I_{front}. Please refer to Table 1 for the list of used symbols.

Table 1. Definitions of the symbols used in Equations (1)–(4).

I_{front}	Global Irradiance on PV Module Front Surface
$I_{b,β}$	Beam component of I_{front}
$I_{d,β}$	Diffuse component of I_{front}
$I_{r,β}$	Reflected component of I_{front}
$β$	PV module tilt angle
I_H	I_{front} for $β = 0$;
$α$	Ground albedo
I_{back}	Incident radiation over the bifacial PV device rear surface
$I_{sc,front}$	Front side component of PV cell short circuit current
$I_{sc,back}$	Back side component of PV cell short circuit current
A_{cell}	PV cell area
$γ$	Incidence angle of the solar radiation on the PV module front
$λ_{Gap}$	PV cell semiconductor bandgap wavelength
EQE_{front}	External Quantum Efficiency for the PV cell front side
EQE_{back}	External Quantum Efficiency for the PV cell back side
$dΩ$	Solid angle element
shadow	Shadow function
A_s	Ground area
T_{amb}	Ambient temperature
T_{module}	PV module temperature
NOCT	Nominal Operating Conditions Temperature

To estimate the solar radiation reaching the rear side of the bifacial PV device, we consider the following. Each point of the not shaded ground is illuminated by the radiation of intensity I_H, which is I_{front} for $β = 0$; the ground element of area dA_s acts as a light source isotropically diffusing, on $2π$ sr, a radiation equal to $(dA_s \cdot I_H \cdot α)$, being $α$ the ground albedo. Therefore, if the module rear surface element of area dA_m sees dA_s under the solid angle $dΩ$, the corresponding optical power will be $(dA_s \cdot I_H \cdot α) \cdot (dΩ/2π)$. Consequently, by computing the integral over the ground whole surface, the incident radiation over the bifacial PV device rear surface (I_{back}) is obtained. However, we also consider the incidence angle of radiation on the receiving surface element dA_m. As it is well-known, when the incident light on a surface is very grazing, the reflectivity tends to 100%; hence, the light is not collected by the mentioned surface. For the interface air—glass-specific case, from the Fresnel equations [38] can be derived that the reflectivity is 50% approximately for an incidence angle of radiation equal to 80°. Therefore, with reference to glass–glass bifacial PV modules, we considered that, for incidence angles equal or larger than $θ_{crit.} = 80°$, the incident radiation is reflected by the module surfaces; hence, it is not collected by the solar cells. Actually, this is a simplified method to take into account optical losses due to PV module encapsulant material reflectivity. Although more accurate and comprehensive methods exist to evaluate such losses (for instance, see Reference [39]), it is noteworthy that the adoption of the above described simplified method led to a good agreement among simulated and experimental results in terms of bifacial module performance, especially by varying the module elevation from the ground, as we proved through the proposed model validation (see Reference [10]). In summary,

the equations used to evaluate the short circuit current values generated by the front and back sides of each bifacial PV cell (denoted as $I_{sc,front}$ and $I_{sc,back}$, respectively) are:

$$I_{sc,front} = A_{cell} \cdot \cos\gamma \cdot \int_{\lambda_{Gap}}^{0} EQE_{front}(\lambda) \cdot I_{front} \cdot d\lambda, \tag{2}$$

$$I_{sc,back} = \int_{A_s} (d\Omega(x,y)/2\pi) \cdot shadow(x,y) \cdot dA_s \cdot \int_{\lambda_{Gap}}^{0} \alpha(\lambda) \cdot EQE_{back}(\lambda) \cdot I_H \cdot d\lambda, \tag{3}$$

where A_{cell} indicates the cell area, γ is the incidence angle of the radiation, λ_{Gap} is the cell semiconductor material bandgap wavelength, EQE_{front} and EQE_{back} represent the External Quantum Efficiency spectra measured for the front and rear cell sides, A_s the ground total area below the cell (divided into differential elements of area dA_s), $d\Omega(x,y)$ is the solid angle (depending on the coordinates x, y of the ground point considered) under which the considered solar cell sees the ground element of area dA_s at the position (x, y), $shadow(x,y)$ is a function (of the considered ground point) representing the shadow projected by the cell (equal to 0, if the ground area is shadowed, 1 otherwise); and $\alpha(\lambda)$ represents the ground albedo. It should be noted that, according to the Equations (2) and (3), $I_{sc,front}$ and $I_{sc,back}$ are calculated as a function of the wavelength λ to consider the dependence on λ of the ground reflectivity and of the solar cell external quantum efficiency values, as measured separately for the front and rear sides of the bifacial solar cell.

Figure 2 shows the external quantum efficiency (EQE) curves for the front and rear surfaces of a bifacial solar cell and the ground reflectivity, used for the calculations performed in the present study. In the case of back illumination, the EQE curve shows a more marked decrease in the blue region of the spectrum compared to the case of front illumination. This is attributed to the different minority carrier lifetimes in the surface layers at the front and at the back, related to the different formation processes of the emitter and base contacts. To take into account the difference between the solar cell EQE and the PV module EQE, the EQE curves of Figure 2 were corrected through a factor δ, close to 1, evaluated by comparing model predictions with experimental data. Such comparison among simulation and experimental data is discussed in detail in our previous work [10], in which we validated the model here proposed by performing outdoor experiments on bifacial PV modules consisting of 4 solar cells in series with the EQE curves shown in Figure 2. In these experiments, we placed the bifacial PV mini-modules over a large area of asphalt in which normal incidence reflectivity spectrum is reported in Figure 2 (green curve). The experimental data concerned PV characteristics as a function of module elevation from the ground, tilt angle, and ground reflectivity (varied by changing the position of a white square back diffuser surrounded by the asphalt). The model and data showed very good agreement with very low deviations (of the order of 1–2%), both in terms of module short circuit current and module maximum power.
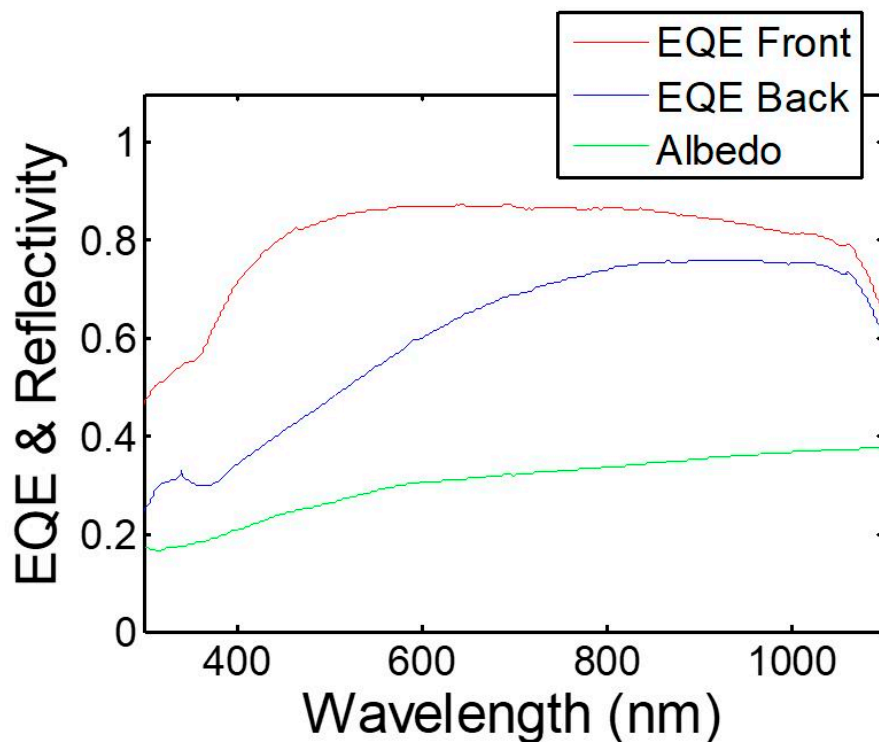
Figure 2. External quantum efficiency (EQE) curves measured for the front and rear surfaces of a bifacial solar cell and ground reflectivity, as a function of the wavelength (λ), used for the calculations in the present study. Such curves were used in Reference [10] to validate the model here described, through experiments performed outdoor on bifacial PV mini-modules consisting of four solar cells in series.

Once the $I_{sc,front}$ and $I_{sc,back}$ values are calculated according to the Equations (1)–(3), the total short circuit current of each bifacial solar cell is determined by adding such values. The overall cell current-voltage (I–V) characteristics are then obtained according to the classical single-diode circuit model of a PV cell [40]. Such a model requires the cell temperature, which is assumed to be the same for each cell and equal to the module temperature T_{module}. T_{module} is calculated as [41]:

$$T_{module} = T_{amb.} + I_{front} \cdot (NOCT - 20)/800. \tag{4}$$

where $T_{amb.}$ represents the ambient temperature (which for all the locations considered in this study was retrieved by an available online public database [42]), I_{front} is the global irradiance at the module front surface (as obtained by the equation (1)), and NOCT represents the Nominal Operating Cell Temperature. The NOCT value was adjusted through the comparison with power data reported in Reference [10]. In the proposed model, we neglect changes of T_{module} due to variations of wind conditions. The wind speed is fixed to the condition of the NOCT definition, i.e., equal to 1 m/s with the PV module at a tilt angle of 45° and its back side open to the breeze.

For the total cell short circuit current, the procedure above described should be repeated cell-by-cell for each bifacial PV module, as it was made in Reference [10], since each cell sees the ground from a different perspective. However, in the present study, we consider relatively large strings of 30 or 60 PV modules, each one composed by 72 cells (hence, for a total number of cells per string equal to 2160 or 4320). Therefore, to simplify the modeling, we neglected the difference among the cells within the same module, and the electrical characteristics of a PV module are evaluated by considering that its cells are all illuminated in the same way. Nevertheless, the uneven distribution of illumination at the rear side is considered among the different modules of the string. This is reasonable since the

differences of solid angle are more relevant among the modules within the string rather than the single solar cells within the same module.

As an example, Figure 3 shows the trend of the solid angle under which each ground element sees the central solar cell of the module at the location ix = 2, iy = 7 (approximately the center) of the considered 30-module fixed string. In such figure, we see also the shadow projected by the string, as calculated at the latitude of Catania, Italy, at 4 p.m. of day number 47 (year 2018).
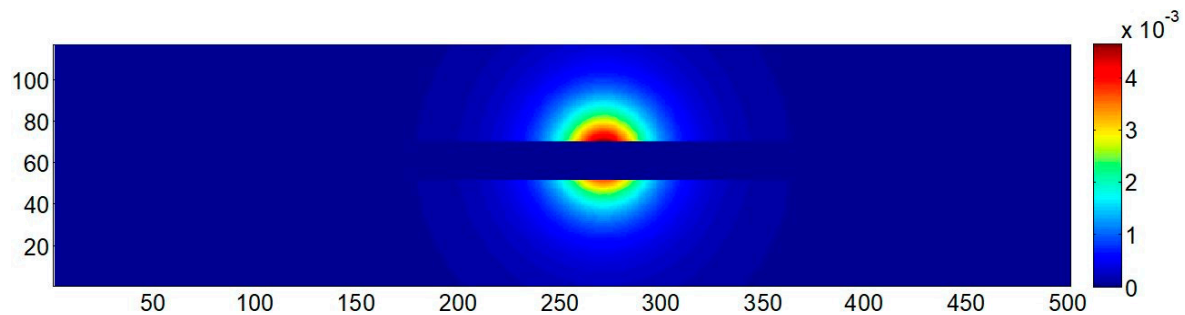
Figure 3. Solid angle values (indicated by the multicolor bar on the right), under which each ground element sees the central solar cell of the module at the location ix = 2, iy = 7 (approximately the center) of the fixed 30-module PV string. The shadow projected by such string, at the latitude of Catania, Italy, at 4 p.m. of day n. 47 of 2018, as simulated by the proposed model, is shown too. The y (east–west direction) and x (north—south direction) coordinates of Figure 1 are represented by abscissa and ordinate of the graph, respectively.

The solar cells considered in this work are bifacial PV cells having a power conversion efficiency of the front side equal to 19.12%, bifaciality factor of 76.6% (calculated as the ratio $(I_{sc,back}/I_{sc,front}) \cdot 100$). Each bifacial PV module considered consists of 72 of such cells, its dimensions are 1 m × 2 m, and its maximum power at the Standard Test Conditions (STC) is equal to 318 W. Moreover, the module power temperature coefficient is equal to 0.47%/°C.

Finally, once the current versus voltage (I–V) electrical characteristics of all PV modules are determined, we determine the I–V electrical characteristics of the considered string by numerically calculating the series of all modules of the string. Figure 4 shows the module I–V characteristics (see red curves) and the corresponding string electrical characteristics (see blue curves with markers), as calculated by the proposed model at time intervals of 1 h, between 7 a.m. and 5 p.m. of day n. 180 at the latitude of Catania, Italy, for both the cases of 30-module fixed string (Figure 4a) and sting with uniaxial horizontal solar tracker (Figure 4b). As we see from the graphs of Figure 4, concerning the current values, the characteristics are almost overlapped between the morning and the afternoon at symmetrical times with respect to midday. At low voltages, the current values for the example at 9 a.m. (see the blue curve with magenta asterisk in the graphs of Figure 4) are similar to those at 3 p.m. (see the blue curve with blue diamond in the graphs of Figure 4). However, near the open circuit voltage (*Voc*), the characteristics are different from each other, as a result of module operating temperature variations, which change the *Voc*.

Furthermore, we note that the I–V characteristics of the strings exhibit quite high slopes at low voltages. This is due to the illumination unevenness of the rear surfaces of the PV modules forming the string and the consequent different values of $I_{sc,back}$ of such modules. For the cases of Figure 4, such an effect is clearly more evident for the case of fixed string.
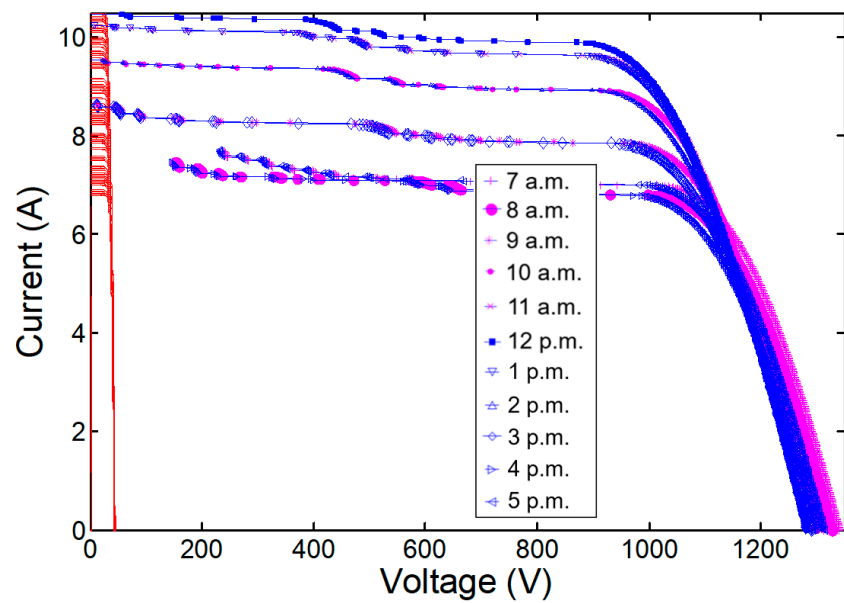
(**a**)
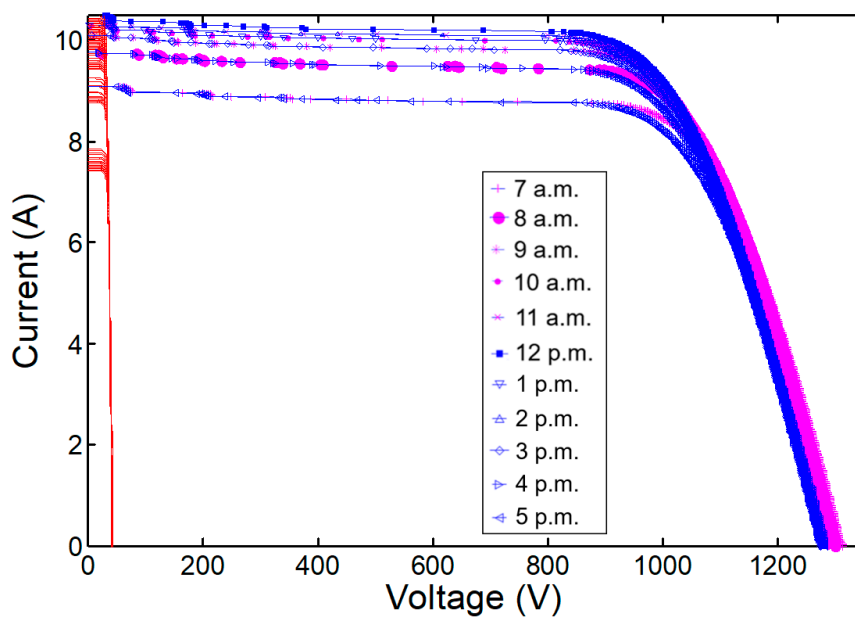
(**b**)

Figure 4. Module I–V characteristics (red continuous curves) and corresponding electrical characteristics of 30-module PV string (blue curves with markers), as calculated by the model proposed, at time intervals of 1 h, between 7 a.m. and 5 p.m. of day n. 180 at the latitude of Catania, Italy, for both the cases of: (**a**) fixed string and (**b**) string with uniaxial horizontal solar tracker.

3. Results and Discussion

3.1. Perimeter Effects

Figure 5 shows the simulated short circuit current trends of the rear sides of the PV string 30 modules, depending on the YB and XA parameters (indicating the side size of the ground zone considered, according to the schematics of Figure 1), for both the cases of fixed string (Figure 5a) and of string with uniaxial horizontal solar tracker (Figure 5b). The results refer to a bifacial PV string at the latitude of Catania, Italy, at 10 a.m. of day number 79 (year 2018). For the case of fixed string,

a tilt angle of 35° (i.e., near to the optimal one for the mentioned latitude) was set for the modules, with XA = 5 m and YB alternately equal to 0 m, 5 m, 10 m, 20 m, as model inputs. Instead, for the string with the mentioned tracker, YB = 5 m and XA alternately equal to 0 m, 5 m, 10 m, 20 m were set as model inputs. For both the considered PV string cases, by increasing the ground zone side size (YB for the fixed string, or XA for the string with tracker, indicated by the direction of the arrows in the graphs), the back photocurrent values of the modules at the string edges increase (for instance, see the back photocurrents of the modules at iy = 1 and iy = 15 for the fixed string, or ix = 1 and ix = 15 for the string with tracker). This is intuitively expected, since the ground zone contributing to the PV string rear side illumination increases too, when YB and XA are increased. Moreover, we note the presence of a saturation. In fact, the upper curves in the graphs of Figure 5 result almost overlapped for the cases of YB (or XA) = 10 m and YB (or XA) = 20 m. This means that, by increasing YB (or XA) over 10 m, the back-photocurrent values of the modules at the string extremities remain almost unchanged. Therefore, YB (or XA) = 10 m seems to be a saturation condition for the perimeter effects, for the analyzed cases. To further clarify such trends, in Figure 6, we show the back-side short circuit current values of the modules at the string edges and at the center, i.e., at the positions iy (or ix) = 1, 7, 15 of both the two rows of the 30-module PV strings, as a function of the YB and XA parameters, for the same case of Figure 5.

From Figure 6, it appears evident the aforementioned saturation effect, for the modules at the extremities (see the curves referred to the modules 1 and 15) of the PV string two rows, both for the fixed string (Figure 6a) and for the string with tracker (Figure 6b). In general, the perimeter effects are quite significant for these modules, as clearly shown by the mentioned graphs. Moreover, we note that the back short circuit currents of the modules at the PV string center approximately (i.e., the modules at the position iy, or ix = 7 of both the string two rows) are sensibly less affected by perimeter effects, compared to the PV modules at the string extremities. In fact, such currents result almost constant by varying the YB (or XA) parameters. This is particularly evident for the case of fixed string (see the green and blue curves of Figure 6a), while, for the string with tracker, a weak increase of back photocurrents is observable also for the modules at the string center (see the green and blue curves of Figure 6b).

To further show the perimeter effect weight, we calculated the ratios defined as $R1 = I_{sc,back,M.1}/I_{sc,back,M.7}$ and $R2 = I_{sc,back,M.15}/I_{sc,back,M.7}$, being $I_{sc,back,M.1}$ and $I_{sc,back,M.15}$ the back short circuit currents of the PV modules at the string edge positions ix (or iy) = 1, 15, respectively, $I_{sc,back,M.7}$ the back short circuit current of the PV modules at the string central position ix (or iy) = 7. Such ratios were evaluated for different solar times for days close to the winter and summer solstice and equinox (January 15th, March 20th, June 15th, September 15th), for both the rows of a string of 30 bifacial PV modules in fixed configuration or with tracker, at the latitude of Catania (Italy). Figure 7 reports the daily averages of *R1* and *R2* as a function of the *YB* parameter for the fixed string (Figure 7a,b), or of the *XA* parameter for the string with tracker (Figure 7c,d).

From such graphs, it appears evident for all the considered days the heavy effect due to the size of the ground perimeter zones on the back photocurrents of the PV modules at the string extremities, for both the cases of fixed string and string with uniaxial horizontal solar tracker. For instance, for the latter string, the average *R2* ratio on March 20th (spring equinox) reaches the considerable value of 2.4 for XA = 10 m. Moreover, also from the graphs of Figure 7, we observe the already noted saturation effect: the average values of *R1* and *R2* saturate for *YB* (or *XA*) over ~10 m.

To estimate the weight on the bifacial gain of the perimeter effects, we evaluated the bifacial gain of each module of a 30-module bifacial PV string as the ratio $(I_{sc,back} + I_{sc,front})/I_{sc,front}$, where $I_{sc,back}$ indicates the module back short circuit current, and $I_{sc,front}$ represents the short circuit current generated by the module front side only. In particular, we calculated the latter ratio for both the fixed string and that with uniaxial horizontal tracker, at the Catania (Italy) latitude, for the most relevant case of ground zone side size (*YB*, or *XA*) equal to 10 m (that is, in the saturation condition previously found).
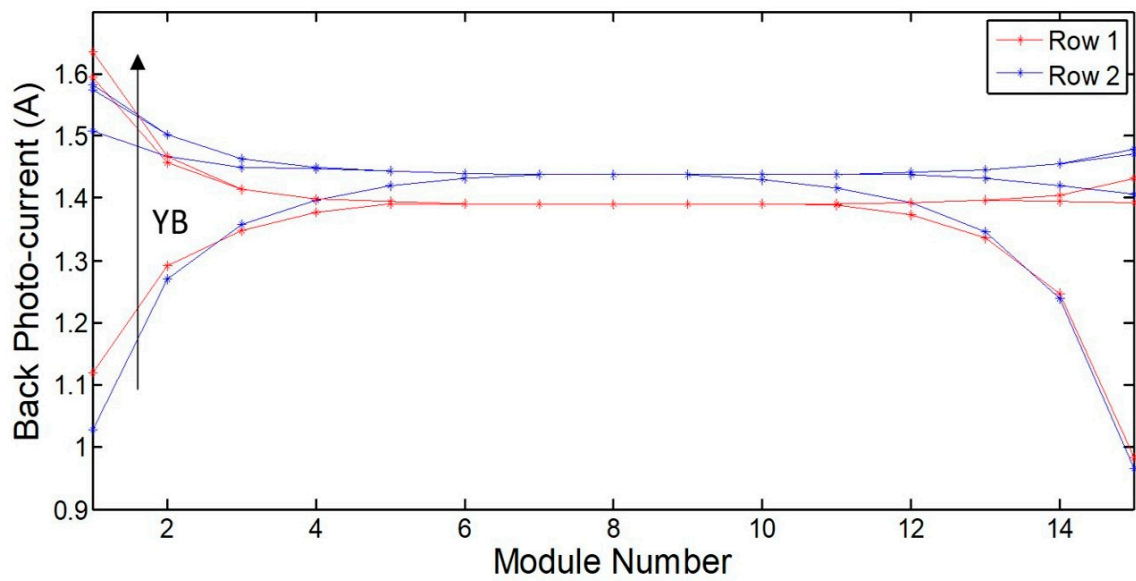
(**a**)
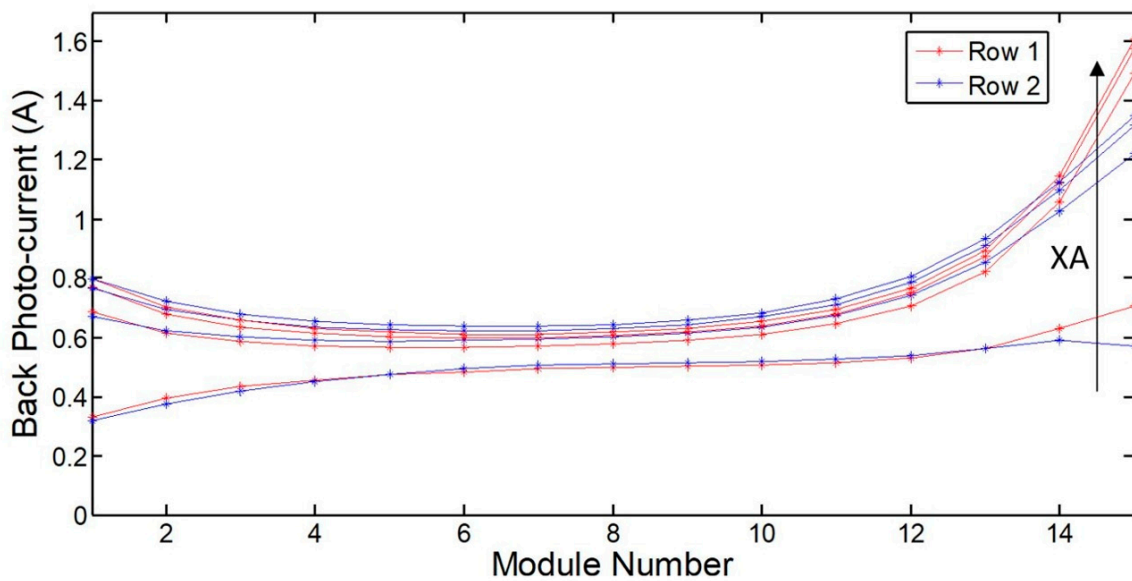
(**b**)

Figure 5. Rear side short circuit current levels for PV strings of 30 modules for the cases of (**a**) fixed string and (**b**) string with uniaxial horizontal solar tracker. The curves are calculated for the parameters YB and XA, respectively, in (**a**,**b**) (see Figure 1 for their definition), equal to 0, 5 m, 10 m, and 20 m. Curves are calculated for Catania at 10 a.m. of day n. 79. The arrows in the graphs indicate the direction of increasing YB (**a**) and XA (**b**).
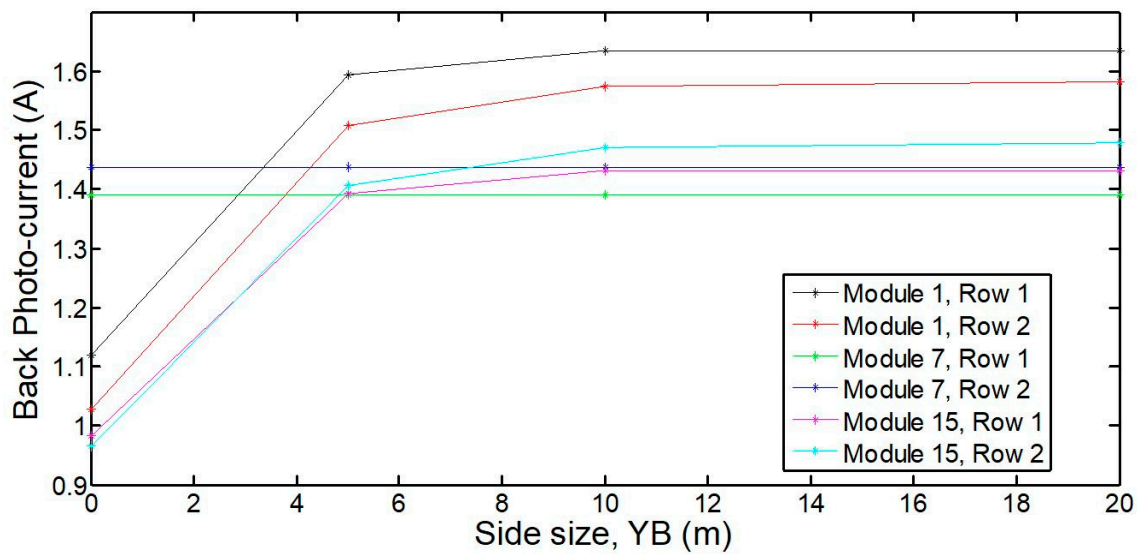
(**a**)
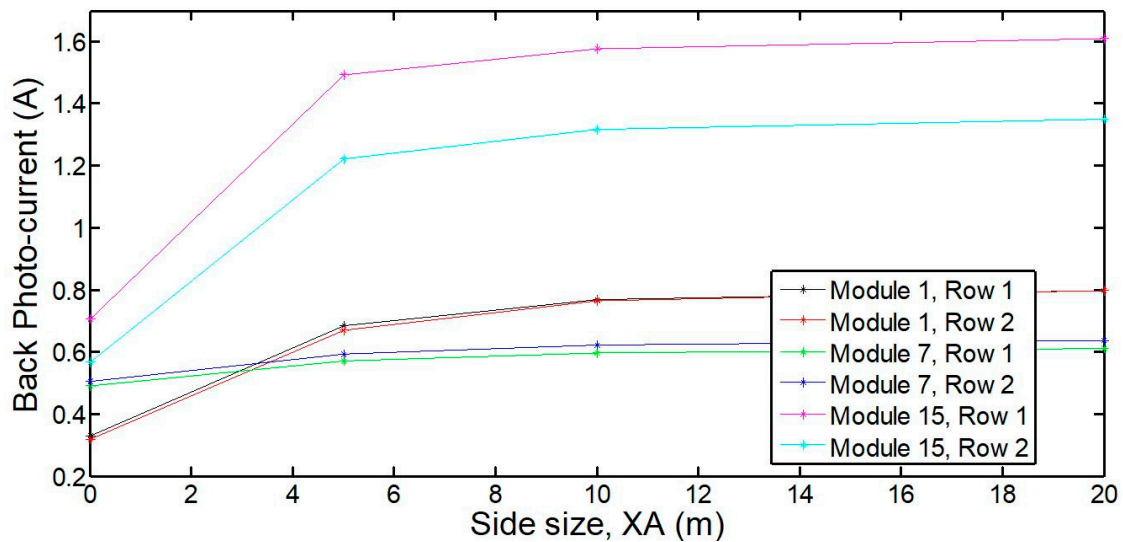
(**b**)

**Figure 6.** Back short circuit current values of the modules at the positions *iy* (or *ix*) = 1, 7, 15 of both the two rows forming the 30-module fixed PV string (**a**) and PV string with uniaxial horizontal solar tracker (**b**), as a function of the *YB* and *XA* parameters, respectively. Note that (see the schematics of Figure 1) the modules at the mentioned positions *iy* (or *ix*) = 1, 15 are at the PV string extremities, while the modules at the position *iy* (or *ix*) = 7 are approximately at the PV string center. The back short circuit current values are calculated by the model, with reference to the Catania (Italy) latitude, at 10 a.m. of day n. 79 (year 2018), considering the same settings used to obtain the graphs of Figure 5.

The bifacial gain for each PV module was calculated for days close to the solstice and equinox, as above for January 15th, March 20th, June 15th, and September 15th. The resulting daily average values of the 30 PV module bifacial gains are reported in Figure 8, for both the cases of fixed string (Figure 8a) and string with tracker (Figure 8b). For both cases, the bifacial gain is evidently affected by perimeter effects. From Figure 8a, we clearly see that the bifacial gains of the modules at the string extremities are remarkably higher than those of the modules at the string center. A similar effect is observed for the string with tracker (Figure 8b). In such a case, the bifacial gain results the highest for the modules at the position *ix* = 15 for both the two rows of the string. This is due to the string shadow

distribution which, during the day, is always shifted towards the north, by favoring on average the modules at the position $ix = 15$, compared to the ones at positions towards north (which are always near to the shadowed ground zone, as, for instance, the modules at the position $ix = 1$). For this reason, the latter modules have, on a daily average, a back photocurrent (hence, a bifacial gain) lower than that of the modules at the position $ix = 15$ and, more in general, at positions towards south.
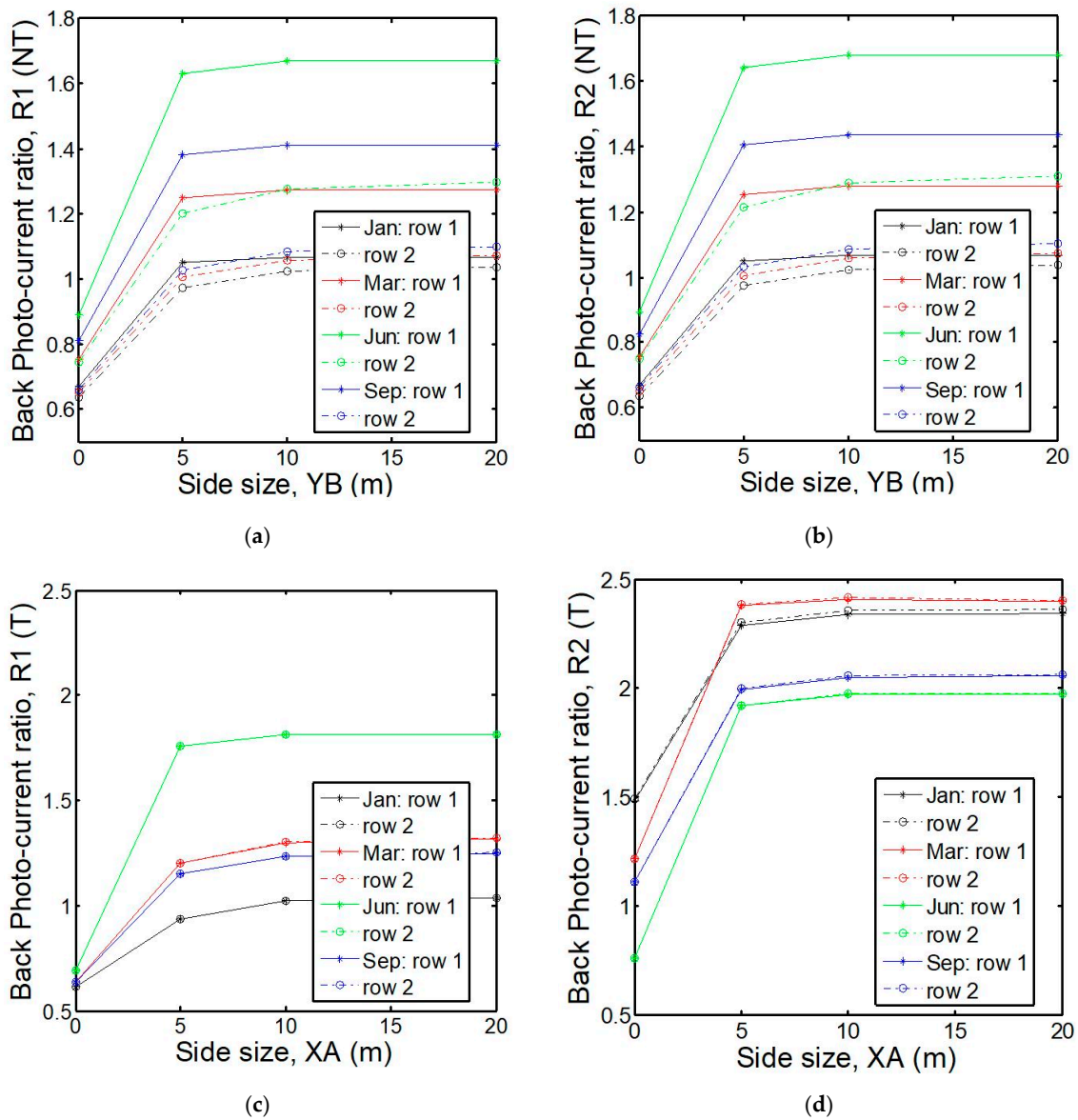
Figure 7. Daily average values of the ratios $R1 = I_{sc,back,M.1}/I_{sc,back,M.7}$ and $R2 = I_{sc,back,M.15}/I_{sc,back,M.7}$ (see the main text for the symbol meaning), as a function of the *YB* and *XA* parameters, for the two rows of the considered 30-module PV strings: fixed string (**a,b**) and string with uniaxial horizontal solar tracker (**c,d**). The mentioned ratio values were calculated by the model, considering the Catania (Italy) latitude, at different solar times of four days of 2018 (January 15th, March 20th, June 15th, and September 15th).
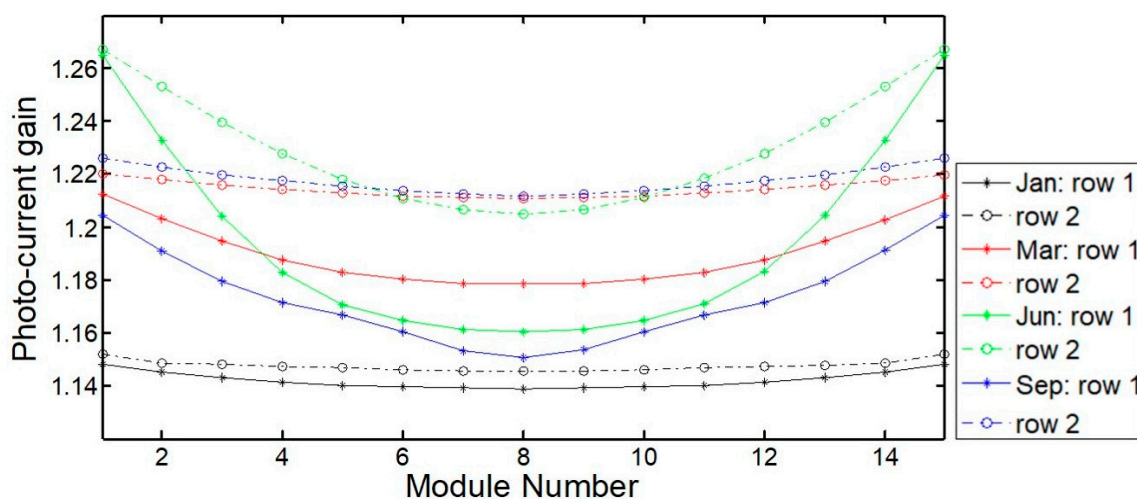
(**a**)
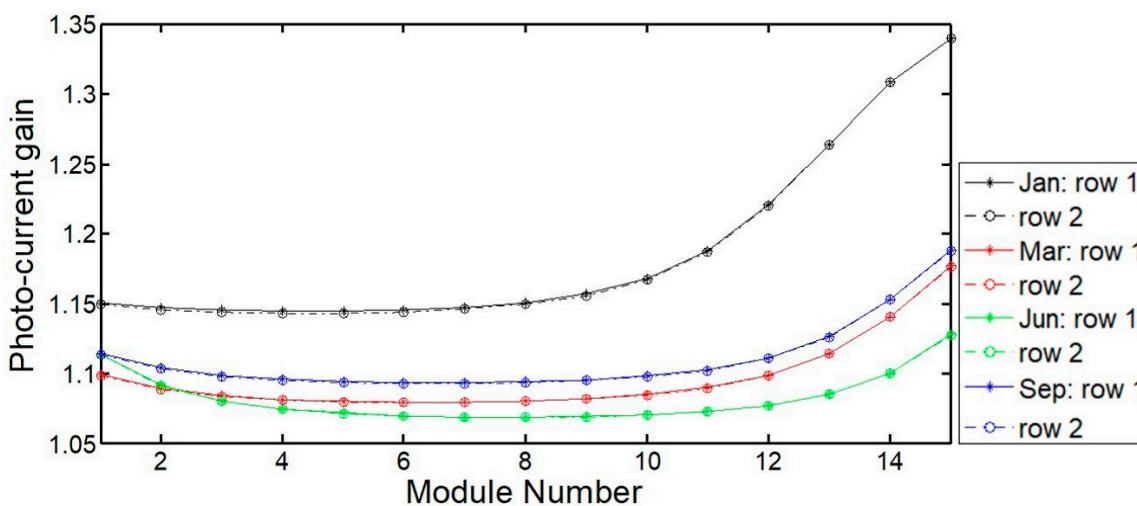
(**b**)

Figure 8. Photo-current gain average values of the 30 modules forming the fixed PV string (see graph in (**a**)) and the PV string with uniaxial horizontal solar tracker (see graph in (**b**)). For each PV module, the mentioned photo-current gain was computed by the model as the ratio $(I_{sc,back} + I_{sc,front})/I_{sc,front}$ (see the main text for the symbol meaning). The calculation was performed for the case of side size equal to 10 m (i.e., the saturation condition for the perimeter effects, according to the results shown in Figures 6 and 7), considering the Catania (Italy) latitude, for different hours of four days of 2018 (January 15th, March 20th, June 15th, and September 15th, i.e., the same days considered to obtain the graphs of Figure 7). For each of such days and for each PV module, the average value of the above defined hourly photo-current gains was determined, as plotted within the graphs here shown.

Figure 9 shows the perimeter effect on the energy generated by a PV string, normalized to the number of modules, for the cases of fixed PV string (with modules nearly optimally tilted for the considered location) and of a PV string with uniaxial horizontal solar tracker, formed by 30 or 60 modules, as obtained by the proposed model for the location of Catania, Italy. On the left (Figure 9a), the specific energy per year is shown; on the right (Figure 9b), the specific energy per day is shown, by considering the day n. 79 (spring equinox) of the year 2018. In such a figure, the lowest three curves refer to the case of fixed PV strings, and the upper three curves refer to the case of strings with tracker. From Figure 9, it is evident that an increase of generated energy of about 10% is achievable by using the solar tracker. Moreover, we note that, in the case of the 30-module PV string, the generated specific energy results higher than that generated by the 60-module PV string. This can be explained

by considering that, with a lower number of modules per PV string, the ratio between the ground area diffusing the light and the string total area (hence, the photocurrent generated by the string rear side) increases; consequently, the overall generated energy increases too. As it has already been observed from the data of Figures 6 and 7, by increasing the considered ground zone side size, the string back-photocurrent, as well as the string energy, initially increases. Then, a saturation of the effect is observed for a side size of about 10–20 m. From Figure 9, such a saturation is evident for the case of the 30-module PV string (for both the cases of fixed string and of string with tracker). The saturation effect in Figure 9 is less evident for the case of the 60 module PV string but still present, as evaluated for side sizes larger than 20 m (calculations not shown for figure clarity).

(**a**)   (**b**)
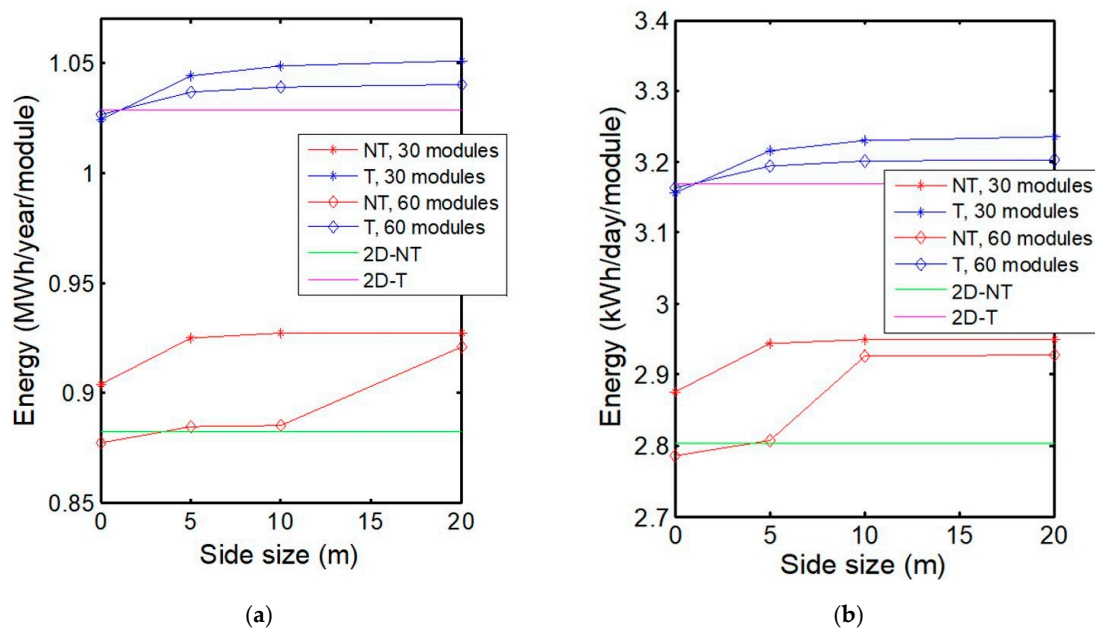
Figure 9. Perimeter effect on the energy (normalized per module) generated by the PV string, for the cases of fixed PV string (see the NT symbol in the legend, acronym of no tracker) and of PV string with uniaxial horizontal solar tracker (see the T symbol in the legend, acronym of tracker), formed by 30 or 60 modules, at the location of Catania, Italy: (**a**) specific energy per year trends, as calculated by the proposed model (considering the year 2018), and (**b**) specific energy per day trends, as calculated by considering the day n. 79 (spring equinox) of 2018. The generated energy is shown as a function of the parameter YB (for $XA = 5$ m) for the case of fixed string and of the parameter XA (for $YB = 5$ m) for the case of string with tracker. Note that the magenta and green continuous lines represent the energy values which would be estimated under the 2D approximation, i.e., the values obtained at the limit for $ny \rightarrow \infty$, $nx = 2$, $YB = 0$, for the case of fixed string; and for $nx \rightarrow \infty$, $ny = 2$, $XA = 0$, for the case of string with tracker (see the schematics of Figure 1).

As comparison, we evaluated the specific energy values which would be estimated under the 2D approximation (green and magenta continuous lines of Figure 9). These are the values obtained at the limit for $ny \rightarrow \infty$, $nx = 2$, $YB = 0$, for the case of fixed string; and for $nx \rightarrow \infty$, $ny = 2$, $XA = 0$, for the case of string with tracker (see the schematics of Figure 1). The PV string behavior for ny (or nx) $\rightarrow \infty$ was simulated by considering the behavior of the central modules (i.e., the ones at the locations iy (or ix) = 30) of the 60-module PV string (without or with tracker). As we clearly see, under the 2D approximation, the generated energy is underestimated; it is reasonable, by considering that, with this approximation, the contribution due to the ground perimeter zones is not computed, as instead it is made through the 3D modeling.

3.2. Latitude Effect

The effect of latitude on the specific energy generated by monofacial and bifacial 30-module PV strings with uniaxial horizontal solar tracker or without any tracker (fixed string), were evaluated, by considering five different geographical locations of the northern hemisphere, from near to the equator to near to the Arctic Circle. As installation sites for the mentioned PV strings, we considered the following locations: Abu Dhabi, United Arab Emirates (geo. coordinates: 24°27′17.2″ N, 54°39′05.9″ E); Be'er Sheva, Israel (geo. coordinates: 31°15′08.3″ N, 34°47′32.1″ E); Catania, Italy (geo. coordinates: 37°26′32″ N, 15°3′47″ E); Freiburg im Breisgau, Germany (geo. coordinates: 48°00′33.7″ N, 7°50′04.6″ E); and Aarhus, Denmark (geo. coordinates: 56°18′26.9″ N, 10°37′40.7″ E).

Figure 10 shows the energy generated, as a function of the latitude. The energy values, shown in this figure for the mentioned PV strings, are normalized to the number of modules. On the left (Figure 10a), the specific energy per year is shown, while, on the right (Figure 10b), the specific energy per day is shown, by considering day n. 79 (spring equinox) of the year 2018. For the cases of fixed PV string and of string with tracker, the parameters *YB* and *XA*, respectively, were set equal to 10 m (that is the perimeter effect saturation condition for a 30-module PV string, according to the results of Figures 6, 7 and 9). Clearly, the bifacial PV system produces significantly more energy than the monofacial one at the same installation conditions. For instance (according to Figure 10a), at the latitude of Catania, Italy, the yearly energy gain due to the adoption of a fixed bifacial PV string compared to a fixed monofacial PV string results about 9% for the relatively low albedo shown by Figure 2. Moreover, the horizontal uniaxial solar tracker gives a clear advantage in terms of generated energy compared to the fixed PV system, of the order of 14.6%, for the monofacial PV string and of about 11.6% for the bifacial PV string. However, such energy yield advantage tends to decrease by increasing the latitude. This fact is consistent with the findings of the study in Reference [26], referred to the case of PV systems equipped with monofacial PV modules. Moreover, we note that the energy gains achievable by using the considered solar tracker is larger for the case of monofacial PV strings compared to the case of bifacial strings, consistent with the results obtained in Reference [29]. However, in this regard, it is important to note that, in the proposed model, the assumed tracking algorithm considers the solar irradiance optimization only for the module front side (i.e., the so-called azimuth optimization), rather than the optimization of the irradiance on both front and back side of the bifacial modules. By changing the tracking algorithm, in order to optimize the total irradiance, i.e., by optimizing the sum of front and back side irradiation, the energy produced by the bifacial PV system with tracker will be further increased. However, we believe that the magnitude of such effect will heavily depend on the particular installation conditions (ground albedo, inclination of the soil, etc.) and is not considered here since we have assumed, in all cases, an ideal condition with a perfectly flat ground with the albedo of Figure 2.

Finally, we note that the energy yield at higher latitudes results in some cases near or larger than that at lower latitudes. For instance, for the one-day case of the spring equinox, day n. 79 (Figure 10b), the energy yield of Catania (point at latitude ≈37.5°) is quite close to that of Abu Dhabi (point at latitude ≈24.5°). This occurs despite generally, for lower latitudes, higher global horizontal irradiance values are observed. Such peculiar energy yield behavior is explained by the different module operating temperatures at the different geographical locations. In fact, the PV module operating temperatures are significantly higher at locations nearer to the equator, as consequence of the higher average ambient temperature [42]. The higher PV module temperature implies a lower energy yield, and this reduces the advantage of the higher solar irradiance. For the simulations here reported, we assumed a temperature coefficient of −0.47%/°C, typical of crystalline and multicrystalline silicon. However, other PV technologies show lower temperature coefficients, and this will mitigate the PV energy yield decrease with temperature.

(a)   (b)
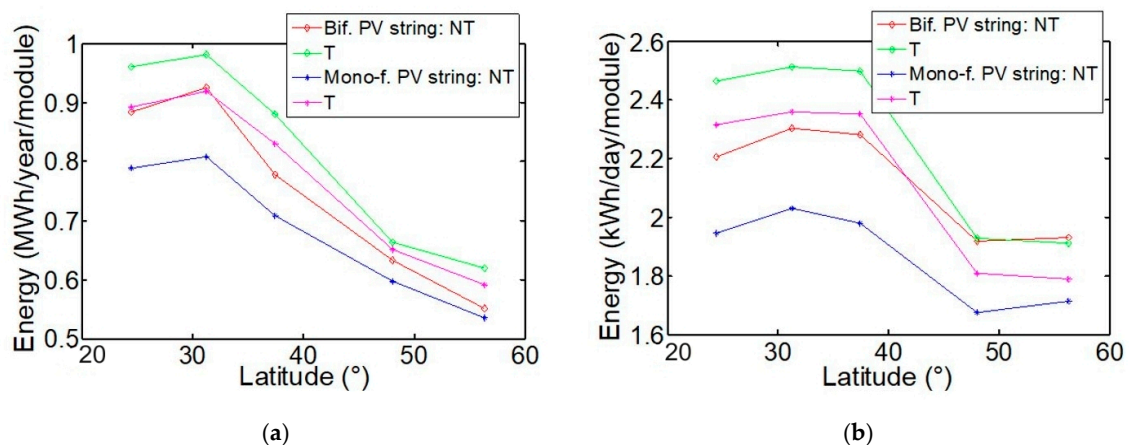
Figure 10. Energy produced, normalized per module, as a function of the latitude, for the cases of: 30-module mono-facial PV stings (i.e., illuminated only from the front side) and 30-module bifacial PV strings, without any solar tracker (fixed string, with module tilt angle equal to the considered latitude) (see NT symbol in the legend) or with uniaxial horizontal solar tracker (see T symbol in the legend), as calculated by the proposed model (considering the five locations specified in the main text): (**a**) specific energy per year; (**b**) specific energy per day, by considering day n. 79 (spring equinox) of the year 2018. For the cases of fixed PV string and of string with tracker, the parameters *YB* and *XA*, respectively, were set equal to 10 m (saturation condition of the perimeter effects).

4. Conclusions

In this work, we presented a 3D model developed for predicting the performance of bifacial PV strings, previously validated with experimental data of PV performance as a function of PV module elevation, tilt, and ground albedo. By using this model, we studied the role played by ground perimeter zones, considering PV strings of 30- or 60-modules organized in two rows, for both the case of fixed installation with optimal tilt, and the case of PV string with uniaxial horizontal solar tracker. The assumed PV string geometries, ground albedo levels, and PV cell EQE curves used for the calculations are reported in Figures 1 and 2, respectively.

The proposed model allowed us to quantify the ground perimeter effects on the performance of the PV strings, in particular, the back-photocurrent of the PV modules at the string extremities, both with and without the solar tracker.

We show that, for a bifacial PV string, the energy yield depends significantly on the size of the perimeter zones surrounding the string, both with and without the use of the tracker. We observe a saturation of energy yield as a function of perimeter size, as shown in Figure 9.

In addition, we studied the energy yield of bifacial and monofacial PV strings as a function of the latitude, by considering five different locations of the northern terrestrial hemisphere (from near to the equator to near to the Arctic Circle). The main results are reported in Figure 10. The PV string energy yield decreases with the latitude and improves by using bifacial systems and/or by adopting trackers, as expected. In particular, by a closer inspection of the results of Figure 10a, for the particular chosen conditions of ground albedo (see Figure 2), we find that, compared to the fixed installation, both in the case of bifacial and of monofacial PV modules, the use of the tracker provides a noticeable advantage, though such advantage is larger in the case of the monofacial PV modules (about +13% higher energy yield on average for the considered geographical positions) compared to the case of the bifacial ones (about +8% on average). Moreover, in general, the bifacial installation provides a large advantage compared to the monofacial one. In particular, we estimate that the bifacial gain results quite large in the case of fixed systems (about +10% on average) and of lower magnitude in the case of systems with tracker (about +5% on average).

References

1. Pujari N, S.; Cellere, G.; Falcon, T.; Hage, F.; Zwegers, M.; Bernreuter, J.; Haase, J.; Yakovlev, S.; Coletti, G.; Romijn, I.; et al. International Technology Roadmap for Photovoltaic (ITRPV) Results 2017 Including Maturity Report 2018 Ninth Edition, September 2018 ITRPV. 2018. Available online: https://pv.vdma.org/en/ (accessed on 16 February 2020).

2. Yusufoglu, U.A.; Lee, T.H.; Pletzer, T.; Halm, A.; Koduvelikulathu, L.; Comparotto, C.; Kopecek, R.; Kurz, H. Simulation of Energy Production by Bifacial Modules with Revision of Ground Reflection. *Energy Procedia* **2014**, 55. [CrossRef]

3. Yusufoglu, U.A.; Pletzer, T.M.; Koduvelikulathu, L.J.; Comparotto, C.; Kopecek, R.; Kurz, H. Analysis of the Annual Performance of Bifacial Modules and Optimization Methods. *IEEE J. Photovolt.* **2015**, *5*, 320–328. [CrossRef]

4. Shoukry, I.; Libal, J.; Kopecek, R.; Wefringhaus, E.; Werner, J. Modelling of Bifacial Gain for Stand-alone and in-field Installed Bifacial PV Modules. *Energy Procedia* **2016**, *92*, 600–608. [CrossRef]

5. Appelbaum, J. Bifacial photovoltaic panels field. *Renew. Energy* **2016**, *85*, 338–343. [CrossRef]

6. Hansen, C.W.; Riley, D.M.; Deline, C.; Toor, F.; Stein, J.S. A Detailed Performance Model for Bifacial PV Modules. In Proceedings of the 33rd European Photovoltaic Solar Energy Conference and Exhibition, Amsterdam, The Netherlands, 25–29 September 2017. [CrossRef]

7. Deline, C.; MacAlpine, S.; Marion, B.; Toor, F.; Asgharzadeh, A.; Stein, J.S. Assessment of Bifacial Photovoltaic Module Power Rating Methodologies—Inside and Out. *IEEE J. Photovolt.* **2017**, *7*, 575–580. [CrossRef]

8. Sun, X.; Khan, M.R.; Deline, C.; Alam, M.A. Optimization and performance of bifacial solar modules: A global perspective. *Appl. Energy* **2018**, *212*, 1601–1610. [CrossRef]

9. Chudinzow, D.; Haas, J.; Díaz-Ferrán, G.; Moreno-Leiva, S.; Eltrop, L. Simulating the energy yield of a bifacial photovoltaic power plant. *Sol. Energy* **2019**, *183*, 812–822. [CrossRef]

10. Ricco Galluzzo, F.; Canino, A.; Gerardi, C.; Lombardo, S.A. A new model for predicting bifacial PV modules performance: First validation results. In Proceedings of the 46th IEEE Photovoltaic Specialists Conference (PVSC 46), Chicago, IL, USA, 16–21 June 2019.

11. Katsaounis, T.; Kotsovos, K.; Gereige, I.; Al-Saggaf, A.; Tzavaras, A. 2D simulation and performance evaluation of bifacial rear local contact c-Si solar cells under variable illumination conditions. *Sol. Energy* **2017**, *158*, 34–41. [CrossRef]

12. Katsaounis, T.; Kotsovos, K.; Gereige, I.; Basaheeh, A.; Abdullah, M.; Khayat, A.; Al-Habshi, E.; Al-Saggaf, A.; Tzavaras, A.E. Performance assessment of bifacial c-Si PV modules through device simulations and outdoor measurements. *Renew. Energy* **2019**, *143*, 1285–1298. [CrossRef]

13. Pvsyst Photovoltaic Software. Available online: https://www.pvsyst.com/help/bifacial_systems.htm (accessed on 16 February 2020).

14. Cai, W.; Yuan, S.; Sheng, Y.; Duan, W.; Wang, Z.; Chen, Y.; Yang, Y.; Pietro, P.; Altermatt, P.P.; Verlinden, P.J.; et al. 22.2% efficiency n-type PERT solar cell. *Energy Procedia* **2016**, *92*, 399–403. [CrossRef]

15. Neville, R.C. Solar energy collector orientation and tracking mode. *Sol. Energy* **1978**, *20*, 7–11. [CrossRef]

16. Nann, S. Potentials for tracking photovoltaic systems and V-troughs in moderate climates. *Sol. Energy* **1990**, *45*, 385–393. [CrossRef]

17. Poulek, V.; Libra, M. New solar tracker. *Sol. Energy Mater. Sol. Cells* **1998**, *51*, 113–120. [CrossRef]

18. Lorenzo, E.; Pérez, M.; Ezpeleta, A.; Acedo, J. Design of tracking photovoltaic systems with a single vertical axis. *Prog. Photovolt.* **2002**, *10*, 533–543. [CrossRef]

19. Abdallah, S. The effect of using sun tracking systems on the voltage–current characteristics and power generation of flat plate photovoltaics. *Energy Convers. Manag.* **2004**, *45*, 1671–1679. [CrossRef]

20. Al-Mohamad, A. Efficiency improvements of photo-voltaic panels using a Sun-tracking system. *Appl. Energy* **2004**, *79*, 345–354. [CrossRef]

21. Bione, J.; Vilela, O.C.; Fraidenraich, N. Comparison of the performance of PV water pumping systems driven by fixed, tracking and V-trough generators. *Sol. Energy* **2004**, *76*, 703–711. [CrossRef]

22. Karimov, K.S.; Saqib, M.A.; Akhter, P.; Ahmed, M.M.; Chattha, J.A.; Yousafzai, S.A. A simple photo-voltaic tracking system. *Sol. Energy Mater. Sol. Cells* **2005**, *87*, 49–59. [CrossRef]

23. Tomson, T. Discrete two-positional tracking of solar collectors. *Renew. Energy* **2008**, *33*, 400–405. [CrossRef]

24. Mousazadeh, H.; Keyhani, A.; Javadi, A.; Mobli, H.; Abrinia, K.; Sharifi, A. A review of principle and sun-tracking methods for maximizing solar systems output. *Renew. Sustain. Energy Rev.* **2009**, *13*, 1800–1818. [CrossRef]

25. Chin, C.S.; Babu, A.; McBride, W. Design, modeling and testing of a standalone single axis active solar tracker using MATLAB/Simulink. *Renew. Energy* **2011**, *36*, 3075–3090. [CrossRef]

26. Bahrami, A.; Okoye, C.O.; Atikol, U. The effect of latitude on the performance of different solar trackers in Europe and Africa. *Appl. Energy* **2016**, *177*, 896–906. [CrossRef]

27. Moradi, H.; Abtahi, A.; Messenger, R. Annual performance comparison between tracking and fixed photovoltaic arrays. In Proceedings of the 2016 IEEE 43rd Photovoltaic Specialists Conference (PVSC), Portland, OR, USA, 5–10 June 2016; pp. 3179–3183. [CrossRef]

28. Vaca, J.S.D.; Ordóñez, F.; Morales, C. Improvements of Photovoltaic Systems by using Solar Tracking in Equatorial Regions. In Proceedings of the 33rd European Photovoltaic Solar Energy Conference and Exhibition, Amsterdam, The Netherlands, 25–29 September 2017; pp. 2352–2357. [CrossRef]

29. Lindsay, A.; Chiodetti, M.; Binesti, D.; Mousel, S.; Lutun, E.; Radouane, K.; Christopherson, J. Modelling of Single-Axis Tracking Gain for Bifacial PV Systems. In Proceedings of the 32nd European Photovoltaic Solar Energy Conference and Exhibition, Munich, Germany, 20–24 June 2016; pp. 1610–1617. [CrossRef]

30. Pelaez, S.A.; Deline, C.; Greenberg, P.; Stein, J.S.; Kostuk, R.K. Model and Validation of Single-Axis Tracking with Bifacial PV. *IEEE J. Photovolt.* **2019**, *9*, 715–721. [CrossRef]

31. Berrian, D.; Libal, J.; Klenk, M.; Nussbaumer, H.; Kopecek, R. Performance of Bifacial PV Arrays With Fixed Tilt and Horizontal Single-Axis Tracking: Comparison of Simulated and Measured Data. *IEEE J. Photovolt.* **2019**, 1–7. [CrossRef]

32. Jain, D.; Lalwani, M. A review on optimal inclination angles for solar arrays. *Int. J. Renew. Energy Res.* **2017**, *7*, 1053–1061.

33. Lorenzo, E. Energy Collected and Delivered by PV Modules. In *Handbook of Photovoltaic Science and Engineering*; Luque, A., Hegedus, S., Eds.; Wiley: Chichester, UK, 2003; p. 905.

34. American Society of Heating, Refrigerating and Engineers. *Air-Conditioning. ASHRAE Handbook, 1985 Fundamentals: An Instrument of Service Prepared for the Profession Containing Technical Information*; The Society: Atlanta, GA, USA, 1985.

35. Global Solar Atlas. Available online: https://globalsolaratlas.info/ (accessed on 16 February 2020).

36. Liu, B.; Jordan, R. Daily insolation on surfaces tilted towards equator. *Ashrae J.* **1961**, *10*, 53–59.

37. Mousavi Maleki, S.A.; Hizam, H.; Gomes, C. Estimation of Hourly, Daily and Monthly Global Solar Radiation on Inclined Surfaces: Models Re-Visited. *Energies* **2017**, *10*, 134. [CrossRef]

38. Wolframresearch scinceworld.wolfram.com. Available online: http://scienceworld.wolfram.com/physics/FresnelEquations.html (accessed on 16 February 2020).

39. Khoo, Y.S.; Walsh, T.M.; Aberle, A.G. Novel Method for Quantifying Optical Losses of Glass and Encapsulant Materials of Silicon Wafer Based PV Modules. *Energy Procedia* **2012**, *15*, 403–412. [CrossRef]

40. Xiao, W.; Dunford, W.G.; Capel, A. A novel modeling method for photovoltaic cells. In Proceedings of the 2004 IEEE 35th Annual Power Electronics Specialists Conference (IEEE Cat. No.04CH37551), Aachen, Germany, 20–25 June 2004; Volume 3, pp. 1950–1956. [CrossRef]

41. Ross, R.G., Jr. Flat-plate photovoltaic array design optimization. In Proceedings of the 14th Photovoltaic Specialists Conference, San Diego, CA, USA, 7–10 January 1980; pp. 1126–1132.

42. Weather Underground. Available online: https://www.wunderground.com/ (accessed on 16 February 2020).